Optoelectronically Innervated Suction Cup Inspired by the Octopus

van Veggel, Stein; Wiertlewski, Michaël; Doubrovski, Eugeni L.; Kooijman, Adrie; Mazzolai, Barbara; Scharff, Rob B.N.

DOI
10.1002/aisy.202400544

Publication date
2025

Document Version
Final published version

Published in
Advanced Intelligent Systems

Citation (APA)
van Veggel, S., Wiertlewski, M., Doubrovski, E. L., Kooijman, A., Mazzolai, B., & Scharff, R. B. N. (2025). Optoelectronically Innervated Suction Cup Inspired by the Octopus. *Advanced Intelligent Systems*, *7*(4), Article 2400544. https://doi.org/10.1002/aisy.202400544

ADVANCED INTELLIGENT SYSTEMS
Open Access
www.advintellsyst.com

Optoelectronically Innervated Suction Cup Inspired by the Octopus

Stein van Veggel, Michaël Wiertlewski, Eugeni L. Doubrovski, Adrie Kooijman, Barbara Mazzolai, and Rob B. N. Scharff**

The suckers on the octopus arm play a pivotal role in the execution of tasks in unstructured environments by providing a means to grip objects as well as perceive the environment through (chemo-)tactile receptors in the suckers. This work presents an octopus-inspired suction cup with high-resolution tactile sensing capabilities using a camera that captures the displacement of markers that are integrated in the suction cup. The orientation of the suction cup with respect to an object surface could be predicted with an average error of 1.97° for latitude and 9.41° for longitude. In a closed-loop control experiment, the orientation of the suction cup with respect to the object surface is estimated by an initial touch and the suction cup is consequently reoriented to approach the object surface in a perpendicular manner. The passive compliance of the suction cup is sufficient to compensate for the prediction error and a seal could be created on all of the objects. In combination with the automated design and manufacturing process, this is a major step toward the deployment of sensory innervated suction cups for motion planning and control of soft continuum robot arms.

1. Introduction

Inspired by octopus arms, researchers have attempted to integrate suction cups on soft continuum robot arms to aid whole-arm manipulation.[1–3] However, compared to the strategies deployed by the octopus to control its arms,[4] the strategies deployed to control their robotic counterparts are computationally expensive and not nearly as effective. A major difference is that most control algorithms for soft continuum robot arms are based on the presence of accurate proprioceptive sensors,[5] whereas the octopus is considered to have poor proprioception. Instead, the octopus heavily relies on the sensory feedback from (chemo-)tactile receptors in its suckers[6] to form a representation of object shape, curvature, and texture[7] as well as coordinate manipulation in the absence of vision.[8] This has motivated research on the sensory innervation of suction cups.[9] However, the resolution of the state-of-the-art sensory innervated suction cups is insufficient for implementation of closed-loop schemes capable of ensuring a perpendicular contact between the suction cup and the object. In addition, the manufacturing process of existing sensory innervated suction cups is often tedious and their design is not easily scaled or otherwise customized to the application needs.

This work presents a bioinspired suction cup design with an integrated high-resolution tactile sensor calibrated for detecting the orientation of the suction cup with respect to an object surface. The working principle of the suction cup is based on the ChromaTouch principle[10–12] and is illustrated in **Figure 1**. Two layers of colored markers are integrated in the suction cup and are captured by a camera. Deformation of the suction cup results in changes in marker position, perceived marker size, and perceived marker color. As a result, the captured image contains rich tactile information regarding the forces acting on the suction cup, as well as the shape and orientation of the object that the suction cup is in contact with. In this work, a convolutional neural network (CNN) was trained to estimate the orientation of the suction cup with respect to the object surface and this estimation was deployed in a closed-loop control scheme to obtain perpendicular contact between the suction cup and object surface. Hereby, this is the first work to demonstrate orientation estimation with a sensory innervated suction cup at a resolution sufficient for ensuring a seal on randomly oriented objects in a

S. van Veggel, E. L. Doubrovski, A. Kooijman
Department of Sustainable Design Engineering
Delft University of Technology
2628 Delft, CE, The Netherlands

S. van Veggel, M. Wiertlewski
Cognitive Robotics Department
Delft University of Technology
2628 Delft, CD, The Netherlands

B. Mazzolai, R. B. N. Scharff
Bioinspired Soft Robotics Laboratory
Istituto Italiano di Tecnologia
16163 Genoa, Italy
E-mail: barbara.mazzolai@iit.it; scharffrbn@ust.hk

R. B. N. Scharff
Division of Integrative Systems and Design
The Hong Kong University of Science and Technology
Clear Water Bay, Hong Kong, China

The ORCID identification number(s) for the author(s) of this article can be found under https://doi.org/10.1002/aisy.202400544.

DOI: 10.1002/aisy.202400544

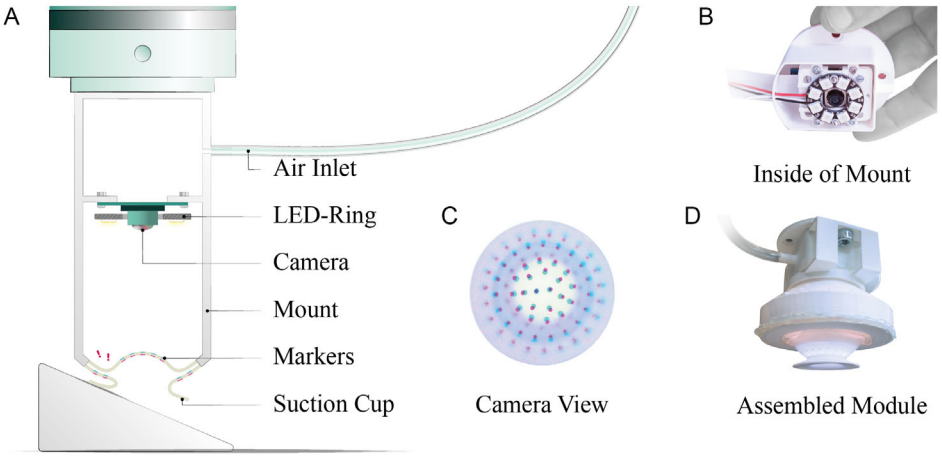

Figure 1. A) Illustration of the working principle of the optoelectronically innervated suction cup. B) Camera and LED ring on the inside of the mount. C) Tactile image taken by the camera. D) Complete module with the suction cup mounted.

closed-loop control scheme. In combination with the automated design and manufacturing process, this is a major step toward the integration of sensory innervated suction cups in soft continuum robot arms for application scenarios as illustrated in **Figure 2**.

The work is organized as follows. Section 1.1 discusses the state of the art in sensory innervated suction cups and camera-based tactile sensors. Next, Section 2 describes the bioinspired design, tactile sensor integration and automated design and manufacturing of the suction cup. Section 3 describes the machine learning methods deployed to estimate the orientation of the suction cup with respect to the substrate based on the tactile images, as well as the experiments that were performed to characterize the performance of the suction cup. The results of the experiments and a demonstration of the orientation estimation in a closed control loop are described in Section 4. Finally, the conclusion is presented in Section 5.

1.1. Related Work

1.1.1. Sensory Innervated Suction Cups

A comprehensive overview of existing works on sensory innervation of suction cups is provided by van Veggel et al.[9] Huh et al.[13] measured the differential pressure between four inner chambers in their suction cup to obtain information about surface curvature, proximity, and texture. Sareh et al.[14] used a fiber optic head in the suction cup to measure proximity and tactile information, for use in motion planning and measuring substrate stiffnesses. Frey et al.[15] used a micro-light detection and ranging (LIDAR) optical sensor next to the suction cup to measure proximity. Giordano et al.[16] integrated mechanochromic materials on a soft suction cup, where three indenters with embedded optical waveguides on top of the suction cup were used to trigger and detect the change in color of the material upon contact between the suction cup and substrate. Lee et al.[17] spray coated four strain sensors on the suction cup's outer wall. They used machine learning algorithms to successfully estimate the object's weight and center of gravity from these input channels. A major limitation of the above-mentioned sensors is their limited resolution. For the application scenario illustrated in Figure 2, the orientation estimation error should be lower than the maximum angle between the suction cup and the object surface for which the suction cup is able to obtain a seal by the passive compliance of the suction cup itself. To address this limitation, Shahabi et al.[18] integrated four

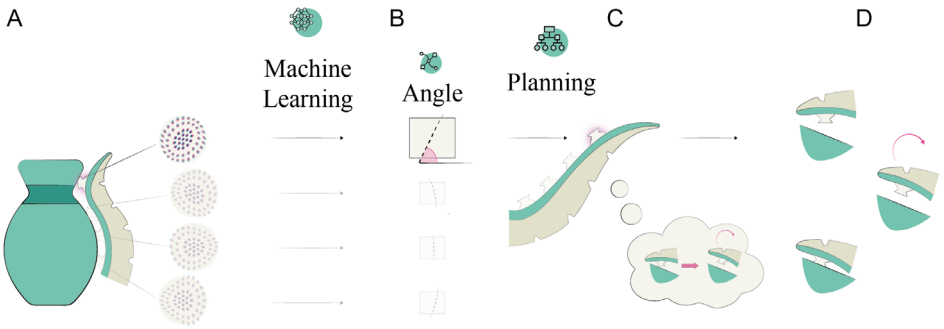

Figure 2. Envisioned application scenario of the sensory innervated suction cup. A) Multiple sensory innervated suction cups are mounted on a soft continuum arm and provide information about the contact through tactile images. B) The tactile images are used to estimate the orientations of the suction cups with respect to the object surface. C) The actuation of the soft continuum arm is adjusted such that the suction cup approaches the object surface in a perpendicular manner and D) a strong attachment is achieved.

microfluidic strain sensors into a silicone suction cup. The angles, directions, stiffnesses, and inclinations of substrates could be estimated from the sensor outputs using a machine learning approach. However, the manufacturing process is tedious and the resistive sensors show significant drift.

Xie et al.[3] placed six suction cups with integrated strain and temperature sensors on an octopus-inspired robot arm.[3] This enabled them to measure contact, attachment and detachment with respect to an object. The contact information was fed back to the operator as haptic feedback using a wearable finger glove. Although this work is promising in the light of integration of the sensory information for soft robot arm control, every suction cup only provides a single resistive sensor signal, making it limited in terms of resolution.

Camera-based tactile sensors are less prone to drift and have a drastically higher resolution. Therefore, the integration of a camera-based tactile sensor in a suction cup has the potential to overcome the existing challenges in sensory innervation of suction cups.

1.1.2. Camera-Based Tactile Sensors

Camera-based tactile sensors provide a robust and low-cost approach to capturing high-resolution tactile information. A camera captures the interior of a medium to collect information about the mechanical interaction between the exterior of the medium and the environment. A critical part of camera-based tactile sensors is the method deployed to convert contact information to a measurable change in the captured red, green, and blue (RGB) image. The Gelsight sensor deploys a red, green, and blue light-emitting diode (LED) to illuminate the back surface of the tactile skin from three different directions.[19] The RGB channels of the camera now provide separate images of the back surface of the tactile skin for each of the lighting directions. Then, photometric stereo technique is used to estimate the surface normals. Although this approach allows for accurate reconstruction of the shape of the object, it requires the addition of markers to enable the detection of shear forces.[20] The use of colored light also forms the basis of the principle of the DIGIT sensor[21] and the tactile sensor by Kappassov et al.[22] A disadvantage of the use of colored light is the difficulty of applying the principle to nonflat tactile surfaces. Gomes et al. addressed this issue through guiding the colored light through a fingertip-shaped elastomer body.[23]

An alternative way to sensory innervate nonflat tactile surfaces is through the embedding of markers on the surface. TacTip deploys a series of geometrically arranged white-tipped pins on the inside of a hemispherical tactile skin.[24,25] The GelForce sensor deploys a tactile skin with two layers of differently colored markers.[26] The lateral deformation of the tactile skin can be estimated through the tracking of the centroids of the markers on both layers. In order to prevent overlap between the markers when a lateral force is applied, the marker density needs to be kept low. This limits the resolution that can be obtained with the sensor. The ChromaTouch tactile sensor addresses this issue through the use of translucent markers on the inner layer, allowing the markers to overlap.[10] Subtractive color mixing now encodes the normal deformation of the membrane, whereas the lateral deformation is obtained through the tracking of the marker centroids. The Chroma Touch principle was demonstrated in a flat[10] and hemispherical tactile skin.[11] However, the manufacturing process comprised several tedious manual steps that also limited the marker density and the precision of the marker placement. This problem was addressed by the adoption of multimaterial additive manufacturing to rapidly manufacture hemispherical ChromaTouch sensors with precise and dense marker placement.[12]

All of the above mentioned marker-based approaches were deployed in a hemispherical tactile surface that is in direct contact with the environment. As only a membrane of uniform thickness separates the markers from the environment, the sensitivity is good and reliable methods exist for reconstructing the deformed membrane shape based on the measured marker displacements.[27] The integration of marker-based tactile sensors in more intricate geometries such as suction cups comes with significant challenges with respect to finding a marker configuration that ensures good sensitivity, fabrication, calibration, and reconstruction. This is the first work to integrate a marker-based tactile sensor in a suction cup. Specifically, this work deploys the ChromaTouch principle in an actively actuated octopus-inspired suction cup using an automated design and manufacturing process.

2. Optoelectronically Innervated Suction Cup

2.1. Bioinspired Design

The *Octopus vulgaris* sucker served as inspiration for the design of the suction cup. A simplified illustration of the octopus sucker is shown in **Figure 3**A. The sucker comprises an upper chamber and a lower chamber connected through an orifice. The lower chamber, or infundibulum, is soft and compliant in nature, enabling it to conform to the substrate shape and create a seal.[28] The upper chamber, or acetabulum, possesses a stiffer structure and is used to produce the volume change required to decrease the pressure through the contraction of radial muscles. A similar morphology was adopted in the bioinspired suction cup (Figure 3B). The lower chamber of the suction cup is used to conform to the substrate, whereas fluidic membrane actuation in the upper chamber of the suction cup replicates the function of the radial muscles in the acetabulum. For convenience, the biological terms are also used to refer to the analogous parts of the suction cup, as indicated in Figure 3. The bioinspired suction cup is actuated by adjusting the pressure of the chamber above the acetabular roof, as illustrated in **Figure 4**. After approaching an object in a neutral state (Figure 4(1)), the pressure in the chamber is increased to inflate the acetabular roof (Figure 4(2)). After the infundibulum comes in contact with the substrate to create a seal (Figure 4(3)), a vacuum is applied to retract the acetabular roof (Figure 4(4)). This increase in internal volume creates a pressure drop and thereby ensures adhesion between the suction cup and the substrate. An advantage of this adhesion mechanism is that the separation of the inner and outer fluids by the acetabular roof prevents contamination of the internal fluidic system, thus making it suitable for both wet and dry conditions. This separation also allows for multiple suction cups

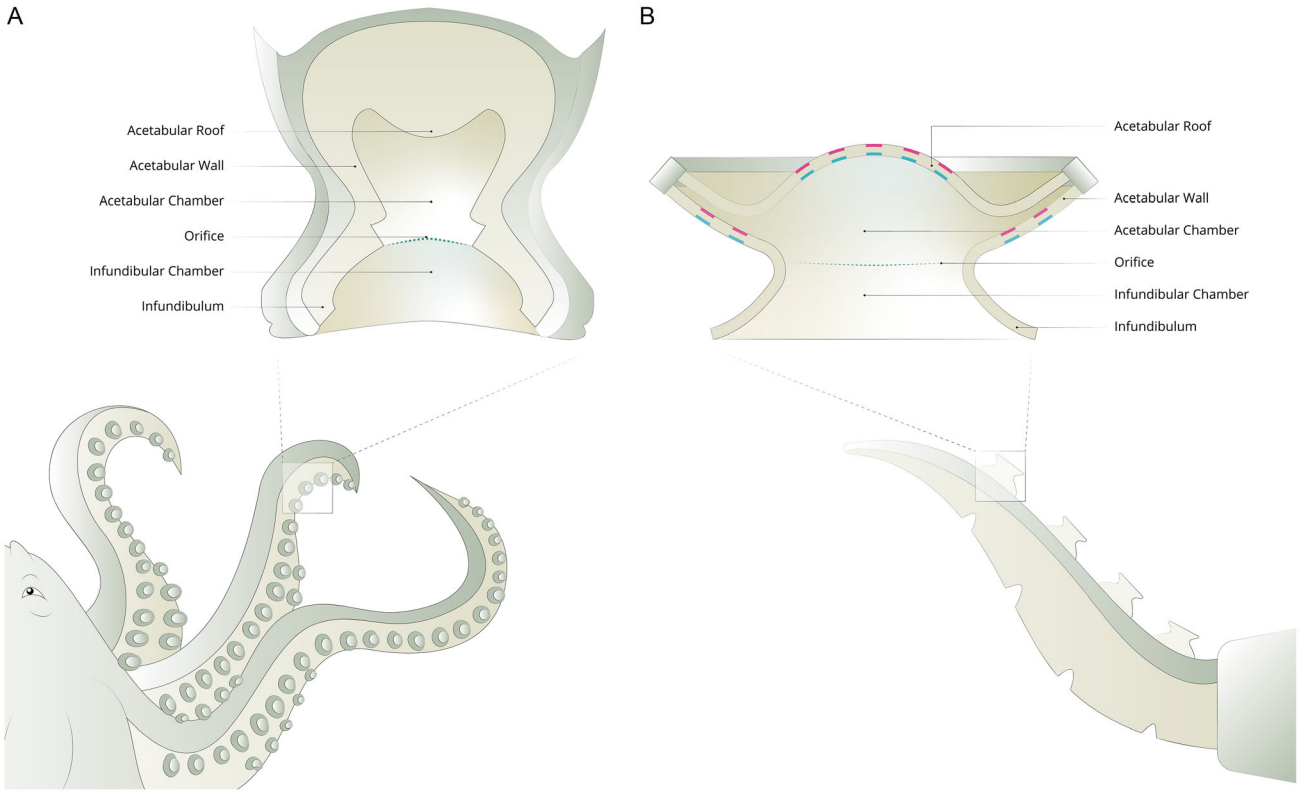

Figure 3. Annotated illustration of A) the *Octopus vulgaris* sucker and B) the bioinspired suction cup design.

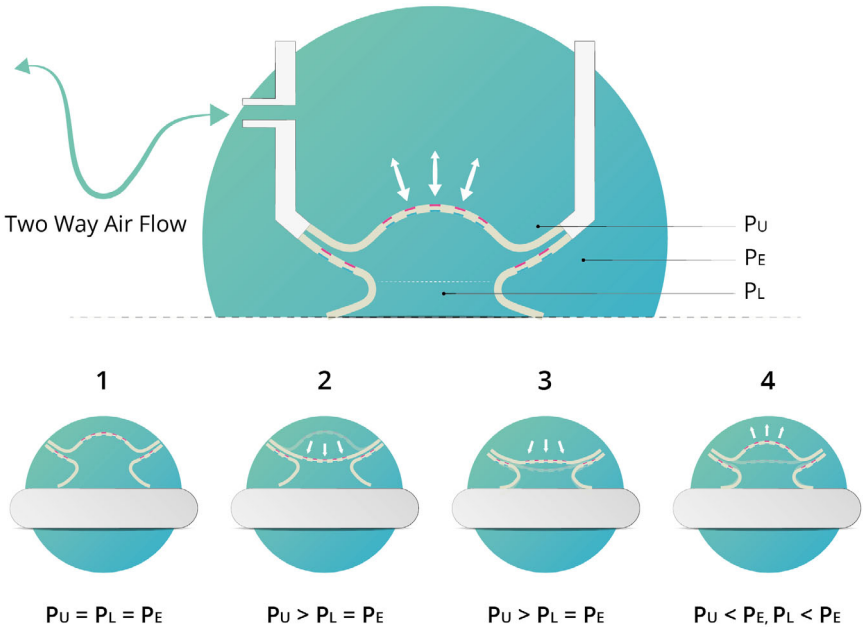

Figure 4. Annotation of pressures in locations relevant for the adhesion process. P_U: Pressure in the chamber above the acetabular roof, directly connected to the fluidic circuit, P_L: Pressure in the acetabular and infundibular chamber. P_E: Environmental pressure. The steps of the adhesion process are shown at the bottom of the figure. 1) Approaching of the substrate with the membrane in a neutral state. All pressures are equal to atmospheric pressure P_E. 2) Activation of the pump to inflate the acetabular roof. P_U increases. P_L is still equal to P_E as no seal has yet been achieved. 3) Pressing the suction cup against the substrate to form a seal. 4) Activation of the pump to create a vacuum above the acetabular roof ($P_L < P_E$). As the acetabular roof retracts, the volume of the chamber inside the suction cup increases and P_U decreases as well ($P_U < P_E$).

to be controlled by a single pump without causing a leakage in the system when one or more of these suction cups do not obtain a proper seal. This property is critical for the application of suction cups along a soft continuum robot arm.

2.2. Tactile Sensor Integration

In addition to its role in the adhesion mechanism, the acetabulum of the bioinspired suction cup plays a critical role in the sensory innervation of the suction cup. As illustrated in Figure 4, ChromaTouch markers are integrated in the acetabular roof as well as the acetabular wall of the suction cup. A camera and LED ring are positioned above the acetabular roof (see Figure 1A). The markers on the acetabular roof are directly perceptible to the camera, whereas the markers on the acetabular wall are indirectly perceptible through the transparant acetabular roof. The marker image captured by the camera when the suction cup is in its neutral position (Figure 4(1)) which is illustrated in Figure 1C. The inflation of the acetabular roof (Figure 4(2)) can be easily detected from the marker image as the markers on the acetabular roof are pushed away from the camera. Next, contact between the infundibulum and substrate becomes apparent from the marker image through the displacement of the markers on the acetabular roof as well as the markers on the acetabular wall (Figure 4(3)). Nonperpendicular contact and contact with nonflat objects result into nonuniform marker response in latitude and longitude, whereas shear forces result into relative movement between the markers on the acetabular roof and the markers on the acetabular wall. Finally, the retraction of the acetabular roof (Figure 4(3)) pulls the markers on the acetabular wall closer to the camera by an amount dependent on the quality of the seal, thereby allowing for the estimation of the adhesive strength based on the marker image.

Per sampling theory, the higher the marker density, the smaller the features of the contact that can be detected. At the same time, the displacement of smaller markers is more difficult to resolve by the camera and leads to a degraded signal-to-noise ratio. One of the advantages of the ChromaTouch approach over counting the number of pixels in black and white markers is that the color provides a decent signal even if only 16 pixels are recruited.[10] Therefore, the marker density can be kept high, ensuring good sensitivity to small features, while keeping the signal-to-noise ratio at a reasonable level.

2.3. Automated Design & Manufacturing

The design and manufacturing process of the suction cup has been largely automated to allow for rapid customization of the suction cup to fit the application needs. The suction cup was parametrically modeled in *Rhino Grasshopper* using a total of 32 parameters. The marker-embedded portions of the acetabular roof and wall were modeled as parts of spherical surfaces to allow for the use of the Deserno Algorithm[29] to uniformly distribute markers over the surface. The algorithm is visualized in **Figure 5**. It takes an arbitrary number of markers N, sphere midpoint location (x, y, z), sphere radius R, and angular domain $[\theta_L, \theta_U]$ as inputs. It then generates a collection of points on the surface, while ensuring the average marker area A_M is constant and $d\theta \simeq d\phi$. This ensures a uniform sampling resolution in the tactile images. The generated points form the centers of cones with their base normal to the spherical surface. For each design variation, the marker density and resolution in the acetabular roof and wall are calculated automatically. The marker densities in the acetabular roof (MD_U) and wall (MD_L) are expressed as the surface ratio between marker area and the total membrane area. The marker resolutions in the acetabular roof (MR_U) and wall (MR_L) are expressed as the number of markers per cm^2.

Additionally, the theoretical pressure change (ΔP) and maximum attachment force (F_{MAX}) are calculated for each design variation. Calculation of these values employs the ideal gas law, assuming a conservation of $P \cdot V$ under a constant gas temperature. In the initial stage of the adhesion process (**Figure 6**A1), the acetabular roof is in its inflated state, the infundibular surface is pressed firmly onto the substrate, and the internal pressure is

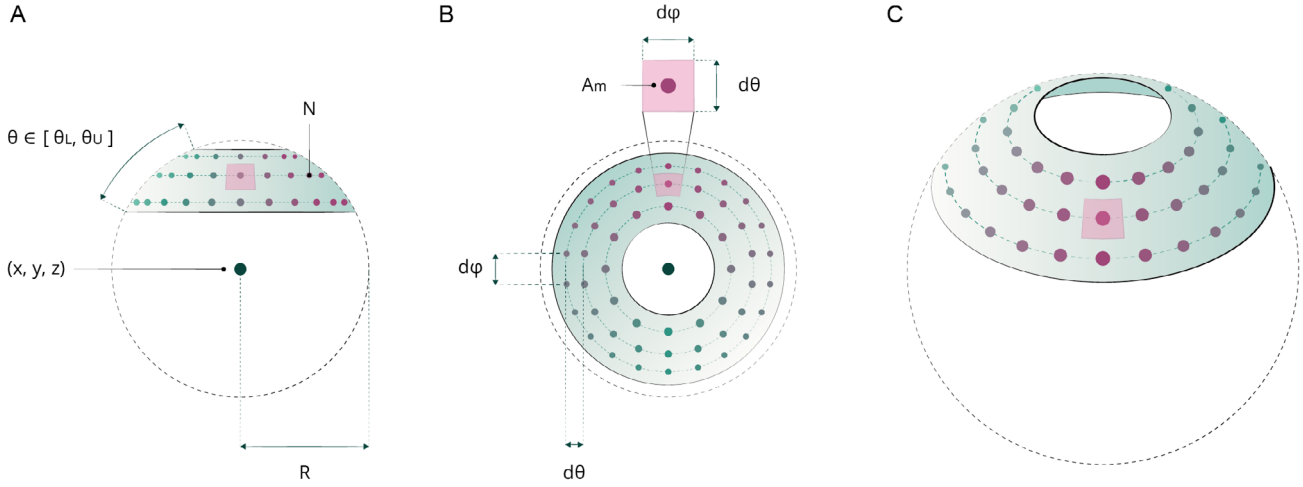

Figure 5. Adapted Deserno algorithm to generate a collection of points on a spherical surface, to form the basis for marker modeling. A) Inputs of the algorithm: Number of markers N, sphere midpoint (x, y, z), sphere radius R, and angular domain $[\theta_L, \theta_U]$. B) Ensuring that the area A_M surrounding each point is equal for all points and $d\theta \simeq d\phi$. C) 3D view of the point collection.

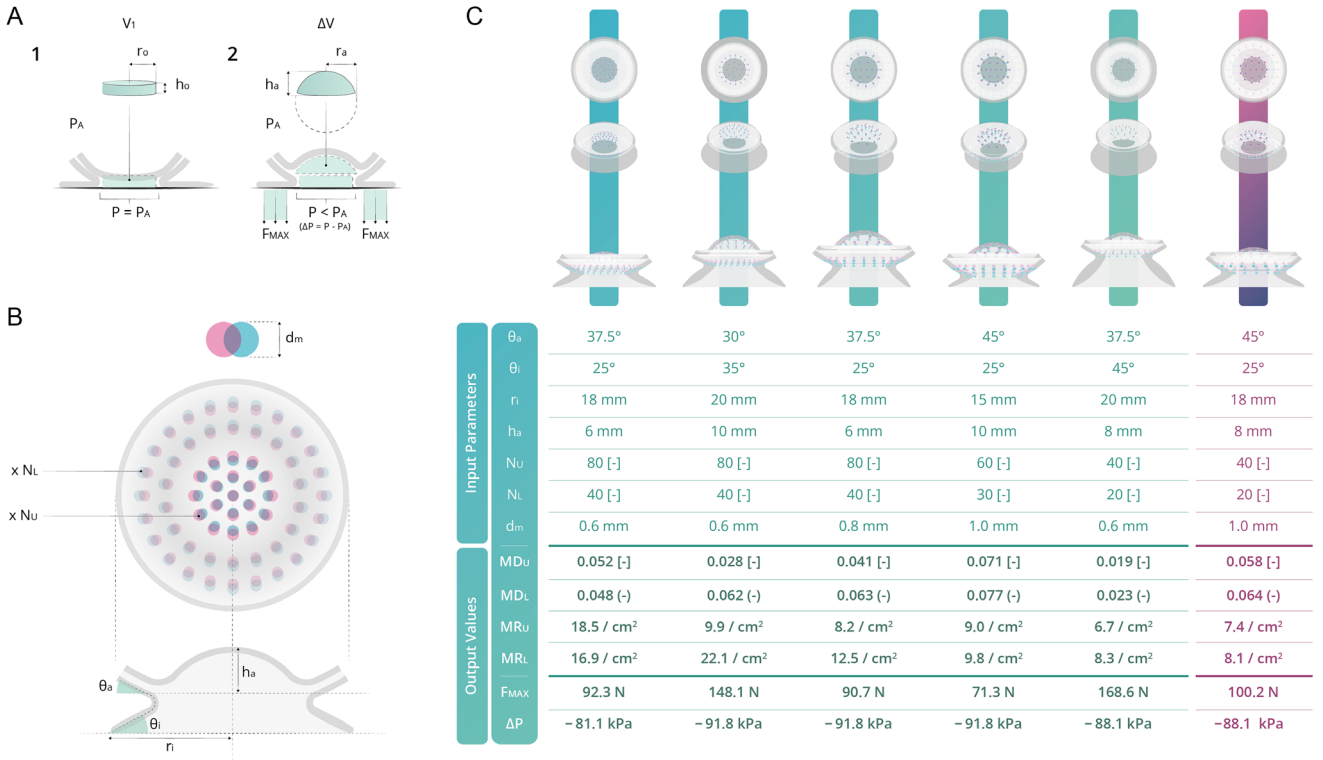

Input Parameters	θ_a	37.5°	30°	37.5°	45°	37.5°	45°
	θ_i	25°	35°	25°	25°	45°	25°
	r_i	18 mm	20 mm	18 mm	15 mm	20 mm	18 mm
	h_a	6 mm	10 mm	6 mm	10 mm	8 mm	8 mm
	N_U	80 [-]	80 [-]	80 [-]	60 [-]	40 [-]	40 [-]
	N_L	40 [-]	40 [-]	40 [-]	30 [-]	20 [-]	20 [-]
	d_m	0.6 mm	0.6 mm	0.8 mm	1.0 mm	0.6 mm	1.0 mm
Output Values	MD_U	0.052 [-]	0.028 [-]	0.041 [-]	0.071 [-]	0.019 [-]	0.058 [-]
	MD_L	0.048 (-)	0.062 (-)	0.063 (-)	0.077 (-)	0.023 (-)	0.064 (-)
	MR_U	18.5 / cm²	9.9 / cm²	8.2 / cm²	9.0 / cm²	6.7 / cm²	7.4 / cm²
	MR_L	16.9 / cm²	22.1 / cm²	12.5 / cm²	9.8 / cm²	8.3 / cm²	8.1 / cm²
	F_{MAX}	92.3 N	148.1 N	90.7 N	71.3 N	168.6 N	100.2 N
	ΔP	−81.1 kPa	−91.8 kPa	−91.8 kPa	−91.8 kPa	−88.1 kPa	−88.1 kPa

Figure 6. A) The simplified geometrical models used for the theoretical force and pressure calculations. A1) Volume of internal chamber before application of the vacuum and A2) after application of the vacuum. B) Visualization where the parameters are located. C) Six suction cup configurations obtained through varying seven geometrical parameters in Rhino Grasshopper. The bottom of the table displays the influence of the parameters on output variables related to sensing (MD = marker density as the surface ratio of total marker area to membrane area, MR = marker resolution in markers/cm^2). The rightmost configuration was selected for the experiments presented in this study.

equal to the atmospheric pressure P_A. The initial volume, V_1, is approximated as a circular disk with height h_o and radius r_o, giving $V_1 = \pi \cdot r_o^2 \cdot h_o$. Activation of the vacuum retracts the acetabular roof upward, increasing the chamber volume between the substrate and the suction cup by ΔV, which is approximated as a spherical cap with height h_a and sphere radius r_a (Figure 6A2). The volume of this cap is calculated as $\frac{1}{3}\pi \cdot h_a^2(3 \cdot r_a - h_a)$. Using the ideal gas law equation $P_A \cdot V_1 = P \cdot (V_1 + \Delta V)$, we calculate P as $P_A \cdot \left(\frac{V_1}{V_1+\Delta V}\right)$. The pressure change is then expressed as $\Delta P = P - P_A$. To calculate the force, the absolute pressure change is multiplied by the infundibular surface area, considering it flat with a surface area of $A_i = \pi \cdot \left(r_o + \frac{r_i - r_o}{\cos(\theta_i)}\right)^2$. Assuming even pressure distribution over the infundibular surface, the theoretical maximum attachment force then becomes $F_{MAX} = A_i \cdot |\Delta P|$.

Figure 6B highlights seven key parameters for the attachment and sensing performance of the suction cup. The number of markers on the upper and lower membrane (N_U and N_L) and the marker diameter (d_m) are the three parameters with the largest influence on MD_U, MD_L, MR_U, and MR_L. The infundibulum angle (θ_i), acetabulum angle (θ_a), infundibulum radius (r_i), and acetabulum height (h_a) are the four design parameters with the largest influence on ΔP and F_{MAX}. To illustrate how each of these seven key design parameters affects the overall design, six designs generated through arbitrarily varying the seven key parameters are highlighted in Figure 6C along with the calculated MD_U, MD_L, MR_U, MR_L, ΔP, and F_{MAX}. The suction cup that was used for the experiments presented in this study is shown on the rightmost side. Although the parametric design tool facilitates design optimization by allowing the user to easily modify the suction cup design, there are trade-offs between different sensor and attachment performance objectives. As a result, the optimal design strongly depends on the application needs. This study focuses on presenting a general approach to sensory innervation that can be applied to the parametric family of suction cup designs. Design optimization for specific applications is beyond the scope of this work.

The manufacturing process of the suction cup is illustrated in **Figure 7**. The top and bottom parts of the suction cup were manufactured by Polyjet additive manufacturing with the *Stratasys J735* (Figure 7A1). This enabled the embedding of the colored markers in both membranes without requiring additional fabrication steps. It also enabled the inclusion of a rigid flange, required for mounting the suction cup during the experiment. The colors of the markers were chosen from the translucent *VeroVivid* family. For the outer markers, *VeroCyan-V* was used. The inner marker layers were fabricated in the more opaque *VeroMagenta-V*. The deformable parts were all fabricated using *Agilus30Clear*, whereas the rigid flange was fabricated using *VeroPureWhite*. The *SUP705* support material was used to support the overhanging features.

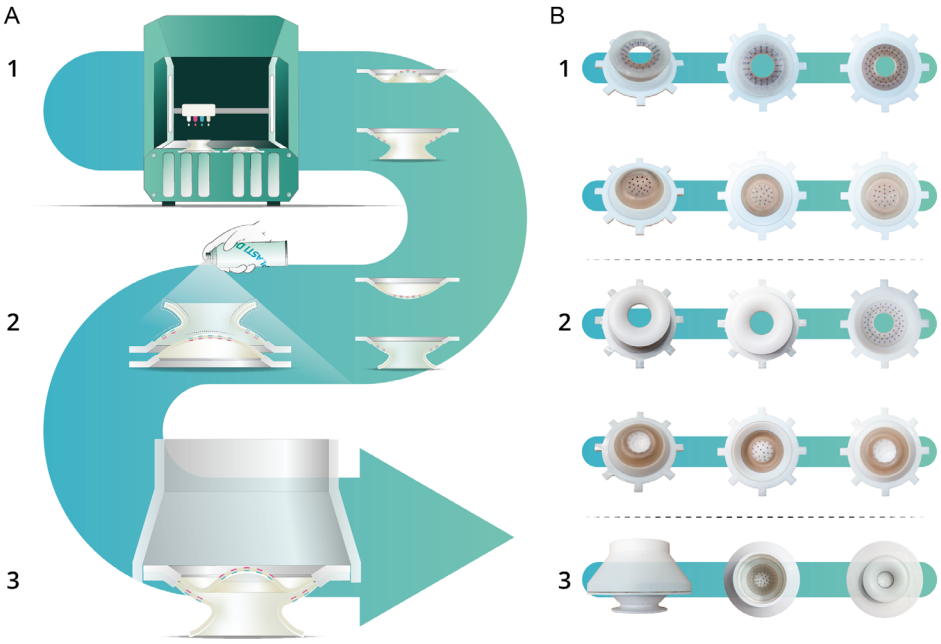

Figure 7. A) Manufacturing steps. A1) Fabrication of top and bottom parts by Polyjet additive manufacturing with the *Stratasys J35*, A2) Spraying *Plasti Dip* rubber onto the highlighted parts. A3) Bonding the top and bottom and attaching them to a polylactic acid (PLA) 3D-printed mount. B) Pictures in different stages of the process. B1) Top and bottom parts before application of *Plasti Dip* and B2) after application of *Plasti Dip*. B3) Assembled module consisting of a top part, a bottom part, and a PLA mount.

After the printing process, a *Plasti Dip* white rubber spray coating was sprayed onto the parts highlighted in Figure 7A2. To preserve the transparency of the acetabular roof's circular edge, this part was masked during the spraying process. The purpose of the coating is to block external light from interfering with the tactile images and to enhance the distribution of light throughout the chamber above the acetabular roof. Fused deposition modeling was deployed to fabricate a mount using polylactic acid (Figure 7A3). This mount facilitates the mounting of the suction cup to the UR5 robotic arm (**Figure 8**) and houses the electronic components.

3. Experimental Section

3.1. Experimental Setup

The experimental setup is illustrated in Figure 8. The electronic components inside the mount included an *Adafruit Neopixel* 8-bit LED ring for the internal lighting, a wide-lens *Raspberry Pi Camera Module V3* for capturing the tactile images, and a *BMP280* barometric pressure sensor for recording the internal pressure. The mount had a pneumatic inlet as well as an inlet for the wiring of the barometric sensor, camera, and LED ring. The distance between the end of the mount and the upper part of

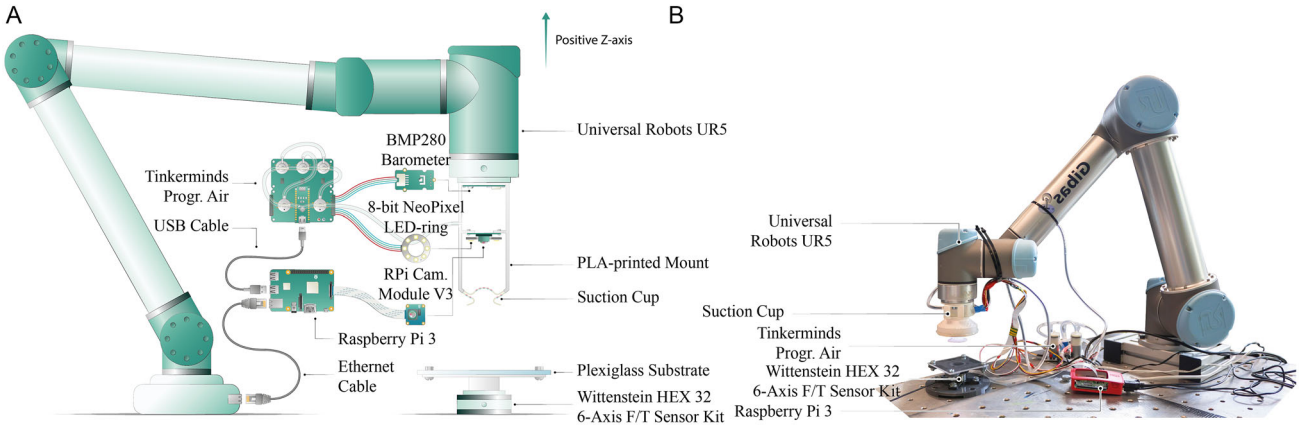

Figure 8. A) Annotated schematic view of the experimental setup. B) Annotated picture of the experimental setup.

the suction cup was 50 mm, which was found to be the minimal focus distance of the camera module. The *TinkerMinds* programmable air device was attached to the pneumatic inlet of the mount. This device consisted of an *Arduino Nano*, two pumps, and three valves. The resulting pneumatic circuit was able to apply both vacuum and compression on several power levels. The camera module and the barometric pressure sensor were connected to a *Raspberry Pi 3* equipped with the lastest version of the *Raspbian* environment. In order to control all hardware components from the *Raspberry Pi* environment, a serial connection was set up between the *Arduino* and the *Raspberry Pi 3* by plugging the *Arduino* USB Cable into the *Raspberry Pi 3*. This enabled the *Raspberry Pi 3* to send serial commands to the *Arduino*. Finally, the mount was attached to a *UR5* robotic arm. For force measurements, an acrylic plate of dimensions 100×100 mm, serving as the substrate, was attached to the *Wittenstein HEX 32* 6-Axis force/torque Sensor kit.

3.2. Experiment I: Basic Functionality

The first experiment focused on the evaluation of the suction cup's basic functionalities. This assessment included two pull-off experiments to evaluate performance under normal and shear forces on a flat surface, as well as pickup experiments involving three different objects. During all experiments, tactile images were captured at every step, which were assessed on their suitability for control-related purposes.

3.2.1. Normal Pull-Off Strength

The objective of the normal pull-off experiments was to determine the indentation and preload that corresponded to the highest normal pull-off force. As normal pull-off force is a commonly used metric for the evaluation of artificial suction cups,[9] measuring it will facilitate an objective performance comparison to other state-of-the-art designs. The preload and pull-off force was measured at six different indentation levels, ranging from 1.0 to 3.5 mm in steps of 0.5 mm. An indentation of 0 mm is defined as the point at which the suction cup exactly touches the acrylic plate but no deformation has yet taken place. The experimental procedure used the setup depicted in Figure 8 and was executed in line with the adhesion process described in Figure 4. During every stage, force and pressure data was collected at 100 Hz and tactile images were obtained at 30 fps. The full process consisted of the following steps. 1) The pump was activated at positive pressure, causing inflation of the acetabular roof. 2) By translating the end-effector of the robot arm in the negative z-direction, the suction cup was moved downward until it reached the determined indentation. This produced a preload force on the substrate. 3) The pump was activated to generate a negative pressure, resulting in retraction of the acetabular roof. The volume increase of the sealed chamber between the suction cup and the substrate generated a pressure drop and led to an attachment force. 4) The robot arm was translated in the positive z-direction at an acceleration of $0.01\,\mathrm{m\,s^{-2}}$ until the maximum velocity of $0.01\,\mathrm{m\,s^{-1}}$ was reached, resulting in the suction cup being pulled off the substrate.

Data postprocessing required time-synchronizing the force—with the pressure—and image data, as they were collected on different devices. This synchronization was based on the moment of indentation, which corresponded to the minimal (negative) force in the z-direction on the substrate and the maximum (positive) pressure in the chamber above the acetabular roof. This is because the indentation caused a slight upward movement of the acetabular roof, resulting in a small pressure peak. The normal pull-off force was then defined as the maximum of the z-component in the force data sequence, while the preload force was defined as the minimum. The execution of the normal pull-off experiment can be observed in Video S1, Supporting Information.

3.2.2. Shear Pull-Off Strength

To proceed with the shear pull-off experiment, the indentation corresponding to the highest normal pull-off force was selected. This experiment followed a similar procedure to the normal pull-off experiment, with one key distinction. Instead of translating the robot arm in the z-direction after activation of the vacuum, the arm was now translated in the x-direction, generating a shear pull-off force. The execution of the shear pull-off experiment can be observed in Video S2, Supporting Information.

3.2.3. Object Pickup Experiments

The pickup experiments also followed the same steps as the normal pull-off experiment, with one distinction. Instead of using the velocity and acceleration of 0.01 and $0.01\,\mathrm{m\,s^{-2}}$ in step 4, these values were now increased by a factor 5 to speed up the pickup of the object. Three objects were used. First, an aluminum block weighing 12.0 g and dimensions $55 \times 40 \times 20$ mm (length $\times$ width $\times$ height) was used. This object was lifted with the center of gravity aligned with the central axis of the suction cup. Second, an elongated aluminum profile weighing 33.0 g and dimensions $150 \times 40 \times 20$ mm was used. This object was lifted with its center of gravity 50 mm from the suction cup central axis. Finally, to assess the adaptability to curved objects, an aluminum cylinder weighing 17.5 g with a 16 mm radius and length of 75 mm was picked up. During all pickup experiments, pressure data was gathered at 100 Hz. The execution of the three pickup experiments can be observed in Video S3, Supporting Information.

3.3. Experiment II: Orientation Estimation

The second experiment addressed the ability to estimate the orientation of the suction cup with respect to the substrate. Differences in orientation between the suction cup and substrate were obtained by deploying the robot arm to position the suction cup in a random orientation before indenting it on the flat substrate. Upon indentation, a tactile image is taken. A CNN, implemented using the *Tensorflow v2.16.1* library, was trained to learn the relationship between these images and the orientation of the suction cup relative to the substrate.

3.3.1. Data Collection Method

The first phase of this experiment involved the collection of orientation-labeled tactile images. A quasistatic approach was adopted, leaving a sufficient amount of time between capturing each image. This ensured that damping and other dynamic effects of the viscoelastic *Agilus30Clear* did not introduce unwanted variations in the tactile images. To eliminate variation introduced by camera focus, the lens distance was set to the minimal value of 50 mm and autofocus was disabled. The resolution of the captured images was 1170×1170 pixels. **Figure 9**A explains how the orientations were defined. A spherical coordinate system was adopted where the center of rotation was located at the intersection of the suction cup's central axis and the circular area defining the edge of the infundibulum (Figure 9A1). After setting a random target orientation (Figure 9A2) in a latitude domain between 0° and 20°, and a longitude domain between 180° and −180° (Figure 9A3), the suction cup was rotated into the target orientation (Figure 9A4). With the goal of making the CNN able to generalize its predictions over varying indentation levels, a randomized indentation between 3.0 and 4.0 mm, with steps of 0.2 mm in between, was generated. Figure 9B1 shows that the zero level was defined as the outer edge of the infundibulum slightly touching the substrate. The suction cup was then translated in the negative *z*-direction of the world coordinate system until the desired indentation was reached (Figure 9B2). The execution of the data collection process can be observed in Video S4, Supporting Information.

Having adopted the system in Figure 9 to define the orientation and indentations, the following steps were executed for the data collection process (**Figure 10**): 1) The robot arm started from a neutral position, with the lowest part of the suction cup positioned 30 mm above the substrate (Figure 10A). 2) The pump was activated at positive pressure, causing inflation of the acetabular roof (Figure 10B). 3) After introducing a waiting period of 2.0 s to allow for damping of vibrations in the membrane, the first image was captured (Figure 10C). 4) The robot arm rotated the suction cup until it reached the desired orientation (Figure 10D). 5) The robot arm translated into the negative *z*-direction until it reached the desired indentation (Figure 10E). 6) After another waiting period of 2.0 s, the second image was captured (Figure 10F).

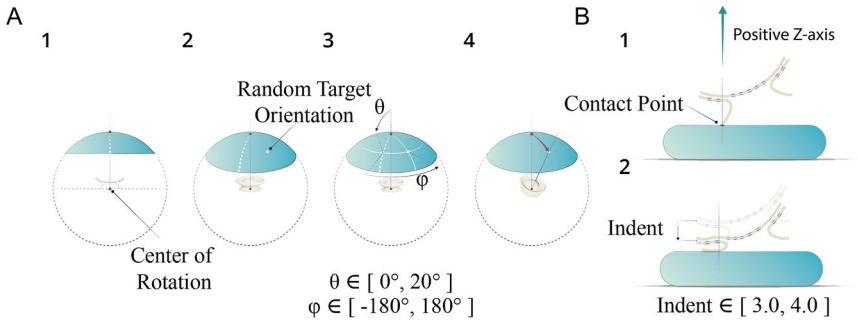

Figure 9. A) Definition of orientation in a spherical coordinate system. A1) The center of rotation is defined as the intersection of the suction cup's central axis and the circular area defining the infundibulum edge. A2,A3) A random target orientation is generated in a latitude domain between 0° and 20° and a longitude domain between 180° and −180°. A4) The suction cup is rotated in the target orientation. B) Definition of the tilted indentation on the substrate. B1) Achieving initial contact with the infundibulum edge. B2) Moving the suction cup in the world negative *z*-direction until the desired indentation is reached.

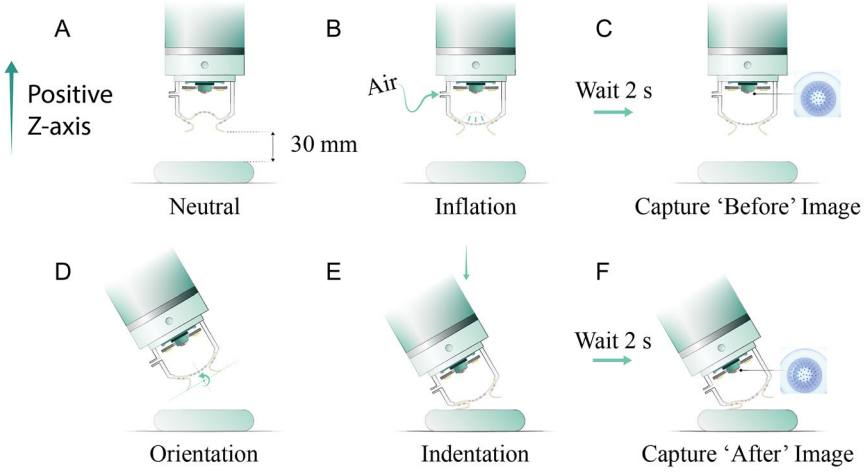

Figure 10. Data collection procedure. A) Neutral position with the lowest part of the suction cup located 30 mm above the substrate. B) Inflation of the acetabular roof. C) After a waiting period of 2.0 s, the "before" image was captured. D) The robot arm rotated the suction cup until it reached the desired orientation. E) The robot arm moved in the negative *z*-direction until the desired indentation was reached. F) After a waiting period of 2.0 s, the "after" image was captured.

3.3.2. Image Postprocessing

The second phase of the experiment involved postprocessing the tactile images before feeding them to a CNN as training data. To ensure solely capturing relevant deformations introduced by the angled indentation and eliminate unnecessary background information, the two images were processed as a single difference image. *Python OpenCV*'s subtract algorithm[30] was employed for this operation. It is important to note that the *OpenCV* subtract algorithm preserves negative pixel outputs, resulting in a lossless difference calculation. The total sequence of postprocessing operations is displayed in **Figure 11**. After saving the difference (Figure 11A), the circle containing only the marker image was cropped out and the image was downsampled to 100×100 pixels to decrease the network training time (Figure 11B). Finally, the downsampled difference image was saved and labeled with the corresponding orientation and indentation values (Figure 11C). In total, 5528 labeled difference images were collected. The execution of the data collection and postprocessing operations can be observed in Video S5, Supporting Information.

3.3.3. Network Architecture & Training

The third phase of the experiment required defining the architecture of the CNN. The network architecture is illustrated in **Figure 12**. The input dimension of the network was set to $100 \times 100 \times 4$, corresponding to the red, green, blue, and alpha (RGBA) values of the tactile images, normalized between 0 and 1. Then, three sequences of convolution with ReLu activation, followed by a 2×2 max pooling layer, were used. The number and dimensions of the kernels deployed at each step are shown at the bottom of Figure 12. The kernels are small 3D matrices used to perform element-wise multiplication followed by a summation as they slide over the input data. The values of the kernels were learnt during the training process such that each kernel extracted a specific feature from the input. The output was flattened and fed into three output nodes. The three output nodes corresponded to the prediction of the latitude value, normalized between zero and one ($\tilde{\theta}$) and the sine and cosine of the longitude value ($\sin(\phi)$ and $\cos(\phi)$). This deconstruction of the longitude value was deployed to eliminate large prediction errors close to a full revolution. The images were randomly divided into training, validation, and test data with a ratio of 0.7, 0.15, and 0.15 respectively. The network was trained in 30 epochs with a batch size of 32, the ADAM optimizer, and the mean square error (MSE) loss function.

4. Results

4.1. Experiment I: Basic Functionality

4.1.1. Normal Pull-Off Strength

The results of the pull-off experiment are shown in **Figure 13**A. On the left, the normal force and the pressure in the chamber above the acetabular roof throughout the adhesion process are plotted. A maximum pull-off force of 9.35 N was achieved at an indentation of 2.0 mm and with a corresponding preload of 22.2 N. This was achieved by activating the fluidic circuit with

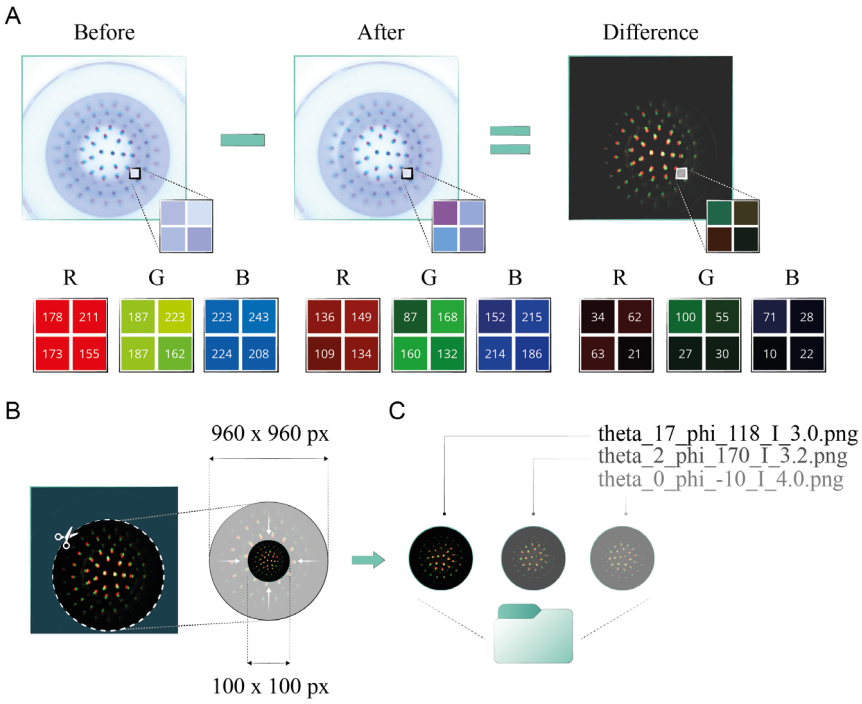

Figure 11. Image of the postprocessing procedure. A) Subtraction of the RGB pixel values of the 'after' from the 'before' image, leaving only the difference. B) Cropping out of the circle containing the markers and downsampling of the image to 100×100 pixels. C) Saving of the image with the corresponding latitude (θ), longitude (ϕ), and indentation (I) labels.

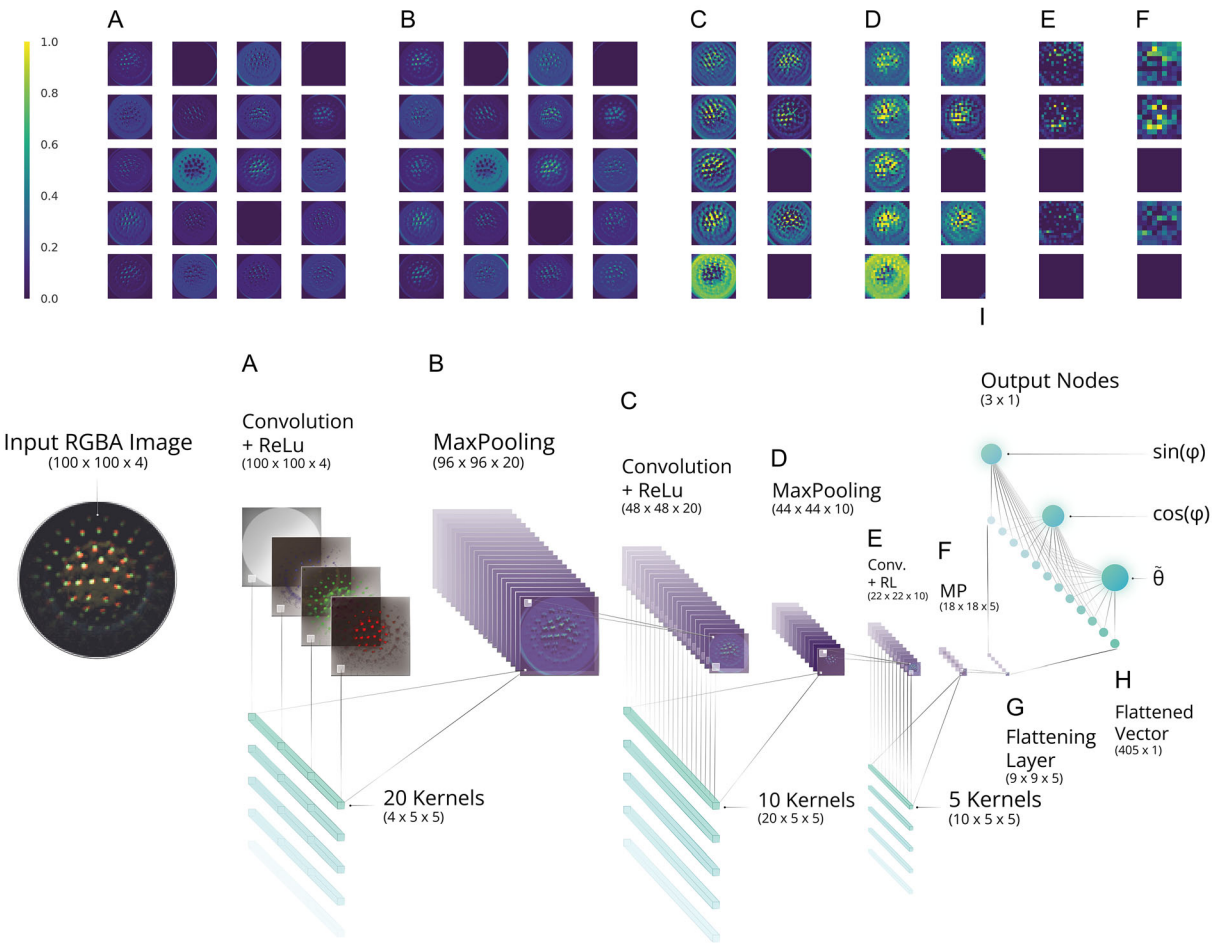

Figure 12. Visualization of the CNN's Architecture. A) The RGBA input image is fed into the first convolutional layer. B) A max pooling operation is performed on the output of convolution. C–F) The network feeds the image into two more sequences of convolution and pooling G,H) The output of the final pooling layer is flattened. I) The flattened vector is fed into three output nodes corresponding to the sine and the cosine of the longitude ($\sin(\phi)$ and $\cos(\phi)$) and the normalized latitude value ($\tilde{\theta}$).

a positive input pressure of 15.28 kPa, followed by a negative pressure of −15.77 kPa. Although this is in line with the state-of-the-art suction cups,[9] it should be noted that this is well below the theoretical maximum force of 100.2 N. When the suction cup is firmly attached to a substrate, there no longer is a gap between most of the infundibular surface and the substrate. Hence, the seal may form near the orifice circumference instead of near the infundibulum circumference. As a result, no negative pressure is applied to most of the infundibular area and that area no longer contributes to generating the attachment force. If it is instead assumed that the pressure is only applied to the orifical area that remains connected to the acetabular area in which the negative pressure is generated, the theoretical maximum force would be 18 N, which is much closer to the obtained results. Other discrepancies could be explained by errors in geometrical assumptions of the calculation and surface roughness of the printed parts and coating resulting in an imperfect seal.

Six moments corresponding to six key stages of the adhesion process are highlighted in the plots and an image of the suction cup at each moment is shown on the right of Figure 13A. A red dashed line is added to each image to indicate the configuration of the acetabular roof at each moment. The tactile images taken at each moment are shown directly below, with additional difference images between the tactile images highlighting the change in tactile image when moving from one stage to the next. It can be seen that especially the changes in membrane configuration upon inflation, suction, and release result in large changes in tactile image (difference image 2–1, 3–2, and 6–5 respectively), whereas differences in load magnitude upon indentation and pull-off result in relative smaller changes (difference image 3–2 and 5−4 respectively).

4.1.2. Shear Pull-Off Strength

The results for the shear pull-off experiments are shown in Figure 13B. When using this same indentation of 2.0 mm for the shear pull-off experiment, the suction cup achieved a shear pull-off force of 5.28 N. The difference image 5–4 demonstrates that the application of shear forces results in a clear difference in tactile image. Moreover, whereas the difference image 5–4 for

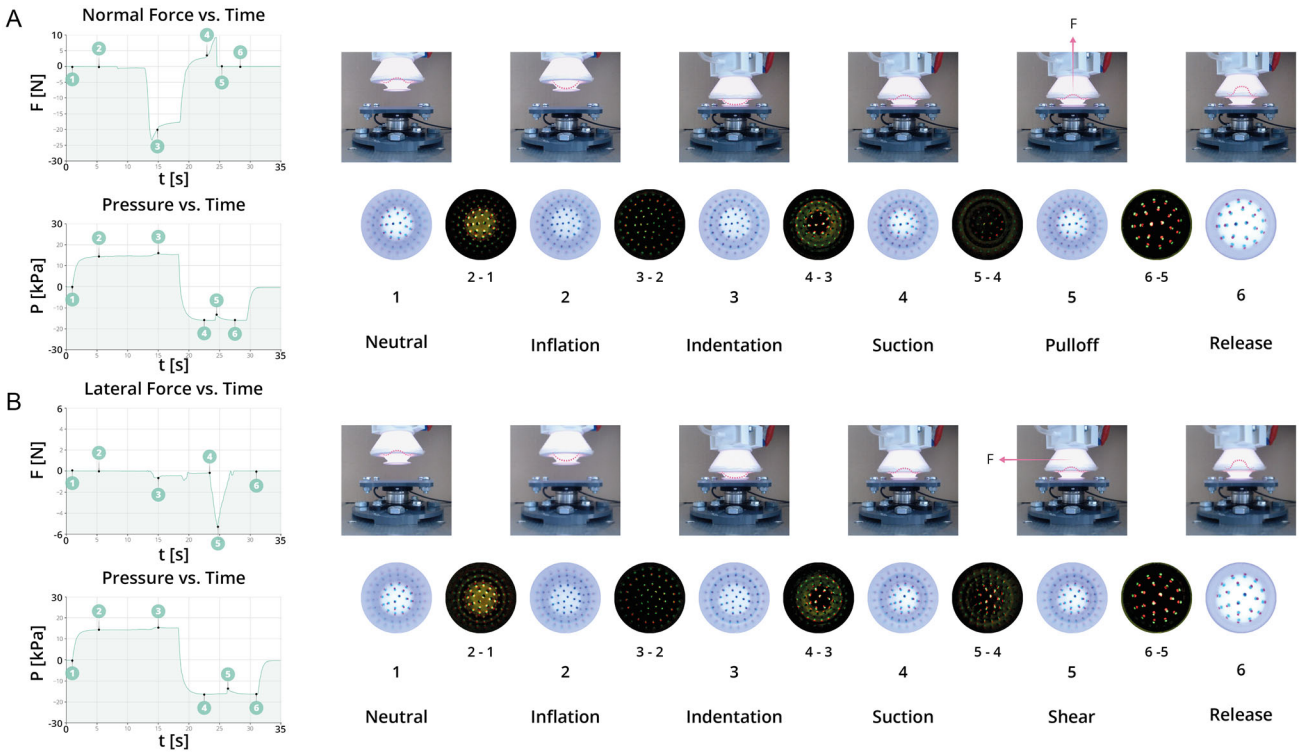

Figure 13. Force and pressure plots for the A) normal pull-off experiment and B) shear pull-off experiment. For both experiments, the tactile images at the 1) neutral, 2) inflation, 3) indentation, 4) suction, 5) pull-off, and 6) release stage are shown, as well as the difference images that highlight the differences between successive tactile images.

the normal pull-off experiment shows a rotationally symmetric response, the difference image 5–4 for the shear pull-off experiment shows a clear asymmetry corresponding to the direction of the applied shear force.

4.1.3. Object Pickup Experiments

Finally, the results of the pickup experiments are shown in **Figure 14**. The pressures in the chamber above the acetabular roof throughout the pickup experiments are plotted on the left, with the five stages of the pickup process shown on the right along with the tactile images at each stage and the difference images between successive tactile images. Despite differences in object shape, weight, and alignment of the center of gravity with the central axis of the suction cup, the suction cup was capable of picking up all objects successfully, highlighting the suction cup's ability to conform to different objects in order to create a seal. Moreover, it was found that different object shapes resulted in clear differences in corresponding tactile images. During the neutral stage and inflation stage, the suction cup is not in contact with the object, and the tactile images for the three different object look similar (Figure 14A–C). Upon indentation, the tactile image taken during the cylindrical object pickup experiment (Figure 14C) shows clear differences from those taken during the flat object pickup experiments (Figure 14A,B), which become most apparent from observing the difference image 3–2 for the three objects. Notably, difference image 3-2 obtained from the tactile images taken during the cylindrical object pickup experiments (Figure 14C) is nonuniform, with small differences where the suction cup is in contact with the top of the cylinder and increasing differences away from this line resulting from the increased deformation of the suction cup conforming to the curved surface. The response for the flat objects with the aligned (Figure 14A) and unaligned (Figure 14B) center of mass is still similar at the indentation and suction stage. However, during the pickup stage, the object with the unaligned center of mass is rotating, resulting in large and nonuniform differences in the tactile image (see difference image 5–4). In contrast, the object with the center of mass aligned with the central axis of the suction cup only shows small and uniform differences between the suction and pickup stage. These changes are caused by the change from a compressive force to a tensile (gravitational) force acting on the suction cup when moving from the suction to the pickup stage.

4.2. Experiment II: Orientation Estimation

4.2.1. Training Results

For the second experiment, the CNN was trained in ≈7 min (14 s per epoch for 30 epochs). This resulted in a training MSE of 0.044 and a validation MSE of 0.042.

Feeding the test set of images to the network resulted in an average absolute latitude (θ) error of 1.97° (9.8%) and an absolute longitude (ϕ) error of 9.41° (2.6%). **Figure 15** displays the error

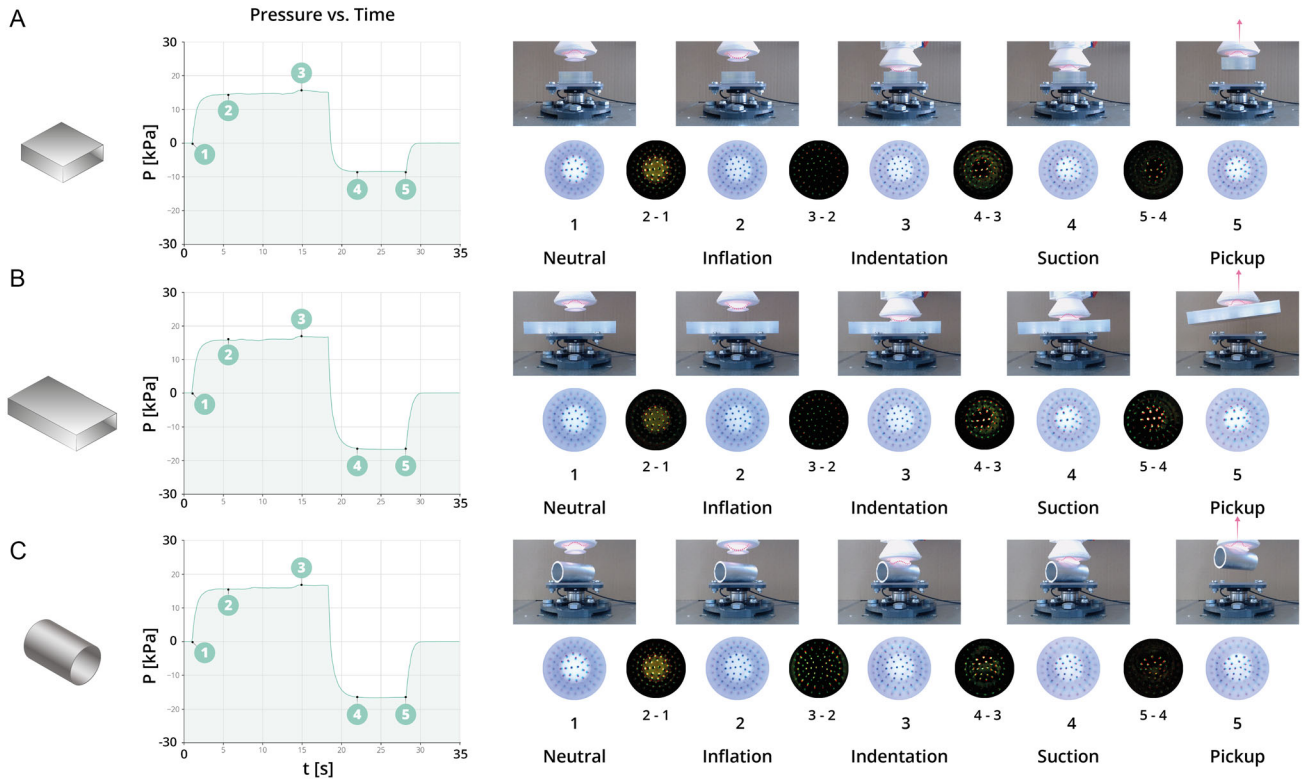

Figure 14. Pressure plots for the pickup experiments of A) an aluminum block with aligned center of gravity, B) a beam with unaligned center of gravity, and C) a cylinder, along with tactile images and difference images at the 1) neutral, 2) inflation, 3) indentation, 4) suction, and 5) pickup stage.

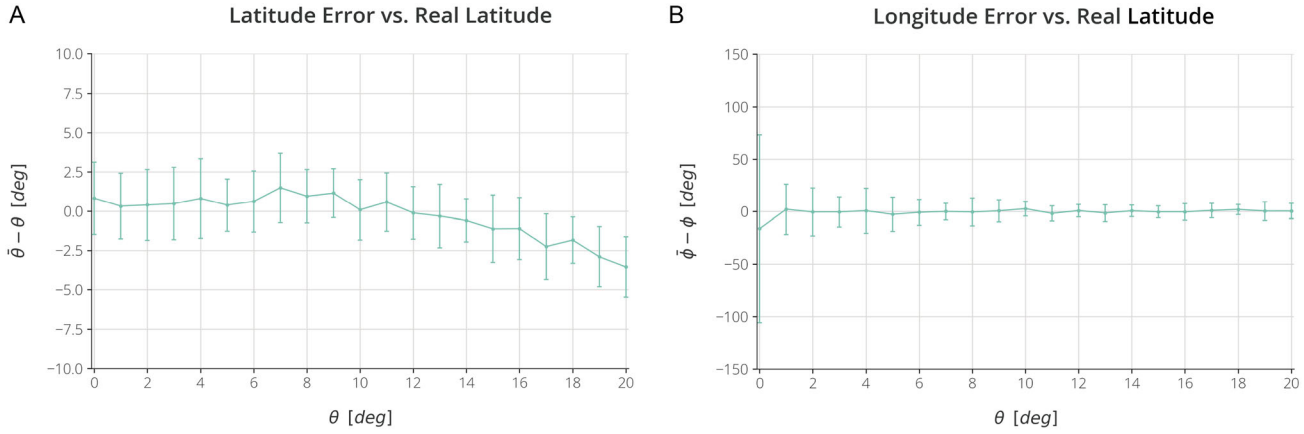

Figure 15. Error bars for A) latitude (θ) and B) longitude (ϕ) prediction errors, Plotted against real latitude values.

bars for both variables against the real latitude values. Next, the generalization behavior over the indentations was evaluated. **Figure 16** displays the error bars representing the prediction error per indentation.

Analyzing the latitude error plot (Figure 15A), a slight decreasing trend is observed as the latitude value increases, passing through zero error at around 12°. This may be attributed to the fact that this experiment involved indirect deformations of the marker membranes, which occur through the transfer of deformation from the suction cup infundibulum. This indirect mechanical filtering effect could result in lower prediction errors for certain "preferred" latitude values, where the chosen architecture exhibits better transfer behavior.

Figure 15B indicates that the prediction errors for longitude display higher variance for a latitude value of zero degrees compared to other values. The cause for this would be that a latitude of zero automatically eliminates the longitude value, as no rotation takes place at all. As latitude increases, more markers undergo displacement, resulting in a higher signal-to-noise ratio and less variation, leading to shorter error bars.

Interestingly, the network's prediction performance did not show a discernible trend based on the magnitude of the

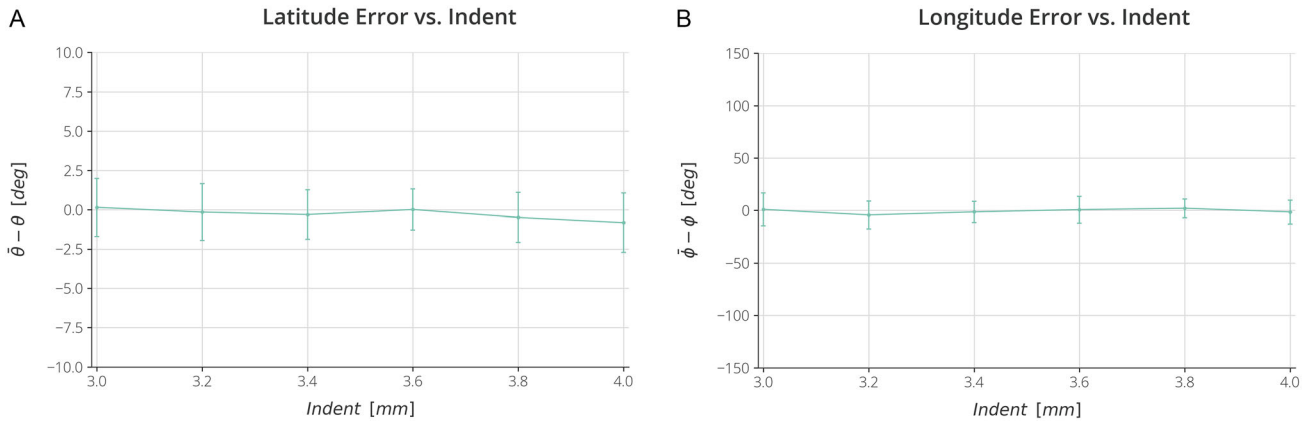

Figure 16. Error bars displaying the A) latitude (θ) and B) longitude (ϕ) prediction errors over each indentation.

indentations (Figure 16). Higher indentations were initially expected to yield a better performance due to increased marker displacement and improved signal-to-noise ratio. The explanation for this might be that the presence of higher indentation introduces more slip between the substrate and the suction cup, contributing to increased variation in the tactile images, which may cancel out the effect of having a stronger signal.

4.2.2. Closed-Loop Control

To verify whether the prediction errors of the CNN were low enough to obtain a seal in real-case scenarios, the trained neural network was deployed in a closed-loop control scheme (**Figure 17**). The suction cup was first used to estimate the relative orientation of the suction cup with respect to the object

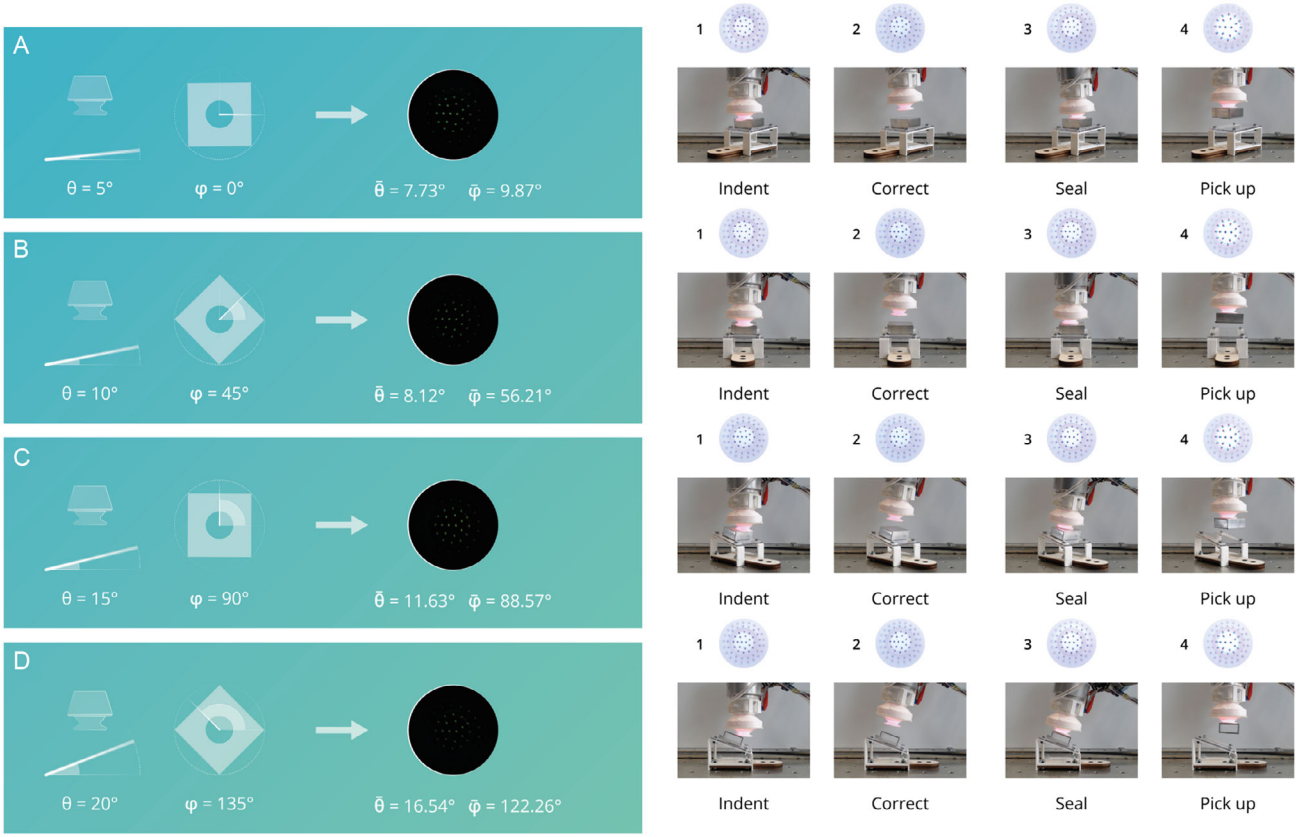

Figure 17. Performance of CNN when using it for live correction of orientation. For A) a latitude (θ) of 5° and a longitude (ϕ) of 0°, B) a latitude (θ) of 10° and a longitude (ϕ) of 45°, C) a latitude (θ) of 15° and a longitude (ϕ) of 90°, D) a latitude (θ) of 20° and a longitude (ϕ) of 135°. The left portion of each subfigure shows the obtained difference image and predicted values. The right portion shows the front view and tactile images in the 1) "indented" stage, 2) "corrected" stage, 3) "sealed" stage, and 4) "picked up" stage.

surface. Then, the suction cup was reoriented such that it approaches the object surface in a perpendicular manner according to the estimated orientation. Both actions are performed with a maximum indentation of 3.5 mm. It was experimentally determined that the maximum angle between the suction cup and the object for which the suction cup is able to obtain a seal due to its passive compliance is 11° at this indentation. This maximum angle can be considered the error tolerance of the system. Objects were placed in four different orientations. The latitude (θ) started at 5° (Figure 17A) and was incremented with 5° (Figure 17B–D) for each successive object. The longitude (ϕ) started at 0° (Figure 17A) and was incremented with 45° for each successive object (Figure 17B–D). The difference images were obtained as explained in Figure 10. The original TensorFlow CNN was first converted to a Tensorflow Lite (TFLite) version to ensure compatibility with the Raspberry Pi. The CNN took 0.66 s to output a predicted orientation from an input image. The suction cup was able to create a seal on, and consequently pick up each of the four objects, demonstrating that the prediction error of the CNN can be overcome by the compliance of the suction cup. The execution of the closed-loop control experiment can be observed in Video S6, Supporting Information.

5. Conclusion

Drawing inspiration from the architecture and sensing abilities of octopus suckers, this work presents an automated design and manufacturing process for a suction cup with high-resolution tactile sensing capabilities. The suction cup exhibited a normal pull-off force of 9.35 N and a shear pull-off force of 5.28 N. It also showed the ability to successfully pick up a flat object, curved object, and a beam with a misaligned center of gravity. Moreover, each of the aforementioned manipulation tasks resulted in distinct tactile images throughout the adhesion process, highlighting the potential for utilizing the obtained tactile information for the design of more sophisticated control strategies. This potential was demonstrated in an orientation estimation experiment. A CNN was able to predict the orientation of the suction cup with respect to an object surface using a 100×100 pixel difference image taken during tilted contact with an average error of 1.97° for latitude (θ) and 9.41° for longitude (ϕ). In a closed-loop control experiment, the unknown orientation of object surfaces was estimated by an initial touch and the suction cup was consequently reoriented to approach the object in a perpendicular manner. It was demonstrated that the compliance of the suction cup was sufficient to compensate for the prediction error and a seal could be created on each of the objects.

In this work, a discrete closed loop control approach was implemented. Upon touching the substrate, a single orientation estimation was made to execute the correction. Future work will focus on implementing continuous closed-loop control, where the suction cup maintains contact with the substrate during reorientation and the estimated orientation is continuously updated to execute the correction. This is expected to enhance performance in dynamic environments as well as on nonflat objects. Moreover, whereas this work demonstrated that contact with objects of different shapes results in distinct tactile images (see Figure 14), the results have focused on demonstrating orientation estimation on flat objects. Future work will focus on calibrating the sensor for estimating object shape, normal force, and shear force as well. This will require a much larger and more varied training dataset. Finally, the design of the suction cup and camera system can be further optimized. Future work will focus on tuning the existing design parameters to optimize for various applications with different requirements regarding size, attachment force, and tactile sensor signal-to-noise ratio. Although the multimaterial additive manufacturing approach also allows for tuning of the material stiffness throughout the suction cup, the current parametric design model does not facilitate the design of suction cups with a nonuniform distribution of material stiffness. Incorporating this functionality in our parametric design model would allow for mimicking the mechanical properties of the octopus sucker to enhance the suction cup attachment performance.[28] The measured normal pull-off forces indicate that the current suction cup is slightly leaking and the negative pressure is not applied across the entire infundibular surface. The octopus sucker contains microdenticles and radial grooves to improve the sealing performance as well as increase the infundibular area to which the negative pressure is applied.[9] Future work will focus on integrating similar features in the parametric suction cup design model. Additionally, the overall size of the system is currently limited by the size and focal length of the camera, hindering integration of the suction cups in soft continuum arms. Hence, future work will focus on miniaturization of the camera system.

Supporting Information

Supporting Information is available from the Wiley Online Library or from the author.

Acknowledgements

The authors thank Yuchen Liang for executing the additional experiments that were required for the revision of this work.

Conflict of Interest

The authors declare no conflict of interest.

Author Contributions

Stein van Veggel: Conceptualization (equal); Data curation (lead); Formal analysis (lead); Formal analysis (lead); Methodology (lead); Visualization (lead); Writing—original draft (lead); Writing—review & editing (supporting). **Michaël Wiertlewski**: Conceptualization (supporting); Investigation (supporting); Methodology (supporting); Supervision (supporting); Writing—review & editing (supporting). **Eugeni L. Doubrovski**: Conceptualization (supporting); Investigation (supporting); Methodology (supporting); Supervision (supporting); Writing—review & editing (supporting). **Adrie Kooijman**: Conceptualization (supporting); Investigation (supporting); Methodology (supporting); Supervision (supporting); Writing—review & editing (supporting). **Barbara Mazzolai**: Conceptualization (supporting); Investigation (supporting); Methodology (supporting); Supervision (supporting); Writing—review & editing (supporting). **Rob B. N. Scharff**: Conceptualization (equal); Investigation (supporting); Methodology (supporting); Supervision (lead);

Writing—original draft (supporting); Writing—review & editing (lead). **Michaël Wiertlewski** and **Eugeni L. Doubrovski** contributed equally to this work.

Data Availability Statement

The data that support the findings of this study are available from the corresponding author upon reasonable request.

Keywords

biologically inspired robots, octopus suckers, suction cups, tactile sensors

Received: July 2, 2024
Revised: October 3, 2024
Published online: January 20, 2025

[1] Z. Xie, A. G. Domel, N. An, C. Green, Z. Gong, T. Wang, E. M. Knubben, J. C. Weaver, K. Bertoldi, L. Wen, *Soft Rob.* **2020**, *7*, 639, pMID: 32096693.
[2] B. Mazzolai, A. Mondini, F. Tramacere, G. Riccomi, A. Sadeghi, G. Giordano, E. Del Dottore, M. Scaccia, M. Zampato, S. Carminati, *Adv. Intell. Syst.* **2019**, *1*, 1900041.
[3] Z. Xie, F. Yuan, J. Liu, L. Tian, B. Chen, Z. Fu, S. Mao, T. Jin, Y. Wang, X. He, G. Wang, Y. Mo, X. Ding, Y. Zhang, C. Laschi, L. Wen, *Sci. Rob.* **2023**, *8*, eadh7852.
[4] G. Sumbre, G. Fiorito, T. Flash, B. Hochner, *Nature* **2005**, *433*, 595.
[5] R. L. Truby, C. D. Santina, D. Rus, *IEEE Rob. Autom. Lett.* **2020**, *5*, 3299.
[6] P. Graziadei, H. Gagne, *J. Morphol.* **1976**, *150*, 639.
[7] J. L. Röckner, M. D. Arellano, L. Zullo, in *Biomimetic and Biohybrid Systems* (Eds: F. Meder, A. Hunt, L. Margheri, A. Mura, B. Mazzolai), Springer Nature Switzerland **2023**, pp. 266–280, ISBN 978-3-031-38857-6.
[8] F. Grasso, *Cephalopod Cognition*, Cambridge University Press **2014**, pp. 94–122.
[9] S. van Veggel, M. Wiertlewski, E. L. Doubrovski, A. Kooijman, E. Shahabi, B. Mazzolai, R. B. N. Scharff, *Adv. Sci.* **2024**, *11*, 2400806.
[10] X. Lin, M. Wiertlewski, *IEEE Rob. Autom. Lett.* **2019**, *4*, 2386.
[11] X. Lin, L. Willemet, A. Bailleul, M. Wiertlewski, in *2020 IEEE Int. Conf. Robotics and Automation (ICRA)*, IEEE, Piscataway, NJ **2020**, pp. 603–609, ISBN 2577-087X.
[12] R. B. N. Scharff, D. J. Boonstra, L. Willemet, X. Lin, M. Wiertlewski, in *2022 IEEE 5th Int. Conf. Soft Robotics (RoboSoft)*, IEEE, Piscataway, NJ **2022**, pp. 896–902.
[13] T. M. Huh, K. Sanders, M. Danielczuk, M. Li, Y. Chen, K. Goldberg, H. S. Stuart, in *2021 IEEE/RSJ Int. Conf. Intelligent Robots and Systems (IROS)*, IEEE, Piscataway, NJ **2021**, pp. 1786–1793, ISBN 2153-0866.
[14] S. Sareh, K. Althoefer, M. Li, Y. Noh, F. Tramacere, P. Sareh, B. Mazzolai, M. Kovac, *J. R. Soc., Interface* **2017**, *14*, 135.
[15] S. T. Frey, A. Haque, R. Tutika, E. V. Krotz, C. Lee, C. B. Haverkamp, E. J. Markvicka, M. D. Bartlett, *Sci. Adv.* **2022**, *8*, eabq1905.
[16] G. Giordano, R. B. N. Scharff, M. Carlotti, M. Gagliardi, C. Filippeschi, A. Mondini, A. Papangelo, B. Mazzolai, *Adv. Intell. Syst.* **2024**, 2400254.
[17] H. J. Lee, S. Baik, G. W. Hwang, J. H. Song, D. W. Kim, B. Y. Park, H. Min, J. K. Kim, J. S. Koh, T. H. Yang, C. Pang, *ACS Nano* **2021**, *15*, 14137.
[18] E. Shahabi, F. Visentin, A. Mondini, B. Mazzolai, *Adv. Intell. Syst.* **2023**, *5*, 2200201.
[19] W. Yuan, S. Dong, E. H. Adelson, *Sensors* **2017**, *17*, 12.
[20] W. Yuan, R. Li, M. A. Srinivasan, E. H. Adelson, in *2015 IEEE Int. Conf. Robotics and Automation (ICRA)*, IEEE, Piscataway, NJ **2015**, pp. 304–311.
[21] M. Lambeta, P.-W. Chou, S. Tian, B. Yang, B. Maloon, V. R. Most, D. Stroud, R. Santos, A. Byagowi, G. Kammerer, D. Jayaraman, R. Calandra, *IEEE Rob. Autom. Lett.* **2020**, *5*, 3838.
[22] Z. Kappassov, D. Baimukashev, Z. Kuanyshuly, Y. Massalin, A. Urazbayev, H. A. Varol, in *2019 Int. Conf. Robotics and Automation (ICRA)*, IEEE, Piscataway, NJ **2019**, pp. 2146–2152.
[23] D. F. Gomes, Z. Lin, S. Luo, in *2020 IEEE/RSJ Int. Conf. Intelligent Robots and Systems (IROS)*, IEEE, Piscataway, NJ **2020**, pp. 9903–9909.
[24] B. Ward-Cherrier, N. Pestell, L. Cramphorn, B. Winstone, M. E. Giannaccini, J. Rossiter, N. F. Lepora, *Soft Rob.* **2018**, *5*, 216.
[25] N. F. Lepora, *IEEE Sens. J.* **2021**, *21*, 21131.
[26] K. Sato, K. Kamiyama, N. Kawakami, S. Tachi, *IEEE Trans. Haptics* **2010**, *3*, 37.
[27] N. J. Ferrier, R. W. Brockett, *Int. J. Rob. Res.* **2000**, *19*, 795.
[28] F. Tramacere, A. Kovalev, T. Kleinteich, S. Gorb, B. Mazzolai, *J. R. Soc., Interface* **2014**, *11*, 20130816.
[29] M. Deserno, How to Generate Equidistributed Points on the Surface of a Sphere, https://www.cmu.edu/biolphys/deserno/pdf/sphere_equi.pdf (accessed: August 2023).
[30] Operations on arrays: Subtract(), https://docs.opencv.org/3.4/d2/de8/group__core__array.html#gaa0f00d98b4b5edeaeb7b8333b2de353b (accessed: August 2023).